MODELING OF HIERARCHICAL CATHODE FOR LITHIUM AIR BATTERIES WITH AQUEOUS ELECTROLYTE

A Thesis Presented to the Faculty of the Graduate School
University of Missouri

In Partial Fulfillment
Of the Requirements for the Degree

Master of Science

---

by
Ning Bi

Dr. Yangchuan Xing, Thesis Supervisor

JULY 2014

The undersigned, appointed by the Dean of the Graduate School, have examined the thesis entitled

MODELING OF HIERARCHICAL CATHODE FOR LITHIUM AIR BATTERIES WITH AQUEOUS ELECTROLYTE

Presented by Ning Bi

A candidate for the degree of Master of Science

And hereby certify that in their opinion it is worthy of acceptance.

Professor Yangchuan Xing

Professor David Retzloff

Professor John Gahl

Professor Stephen Montgomery-Smith

ACKNOWLEDGEMENTS

I would like to express my great appreciation to Dr. Xing for his valuable and constructive suggestions during the planning and development of this research work. His patient guidance, enthusiastic encouragement and useful critiques of this research have helped me a lot. I would like to thank Dr. John Gahl, Dr. David Retzloff and Dr. Stephen Montgomery-Smith for their willingness to be members of my thesis committee as well as the knowledge learned from them in class which helped me a lot for the research.

I would also like to extend my thanks to Yunfeng Li and Litao Yan for their support, help and encouragement throughout my study. I would like to express my appreciation to the staff of chemical engineering department.

Finally, I wish to give my special thanks to my parents and my girlfriend. Their company, encouragement and support give me strength and self-confidence during my hard times.

TABLE OF CONTENTS

LIST OF ILLUSTRATIONS

LIST OF TABLES

MODELING OF HIERARCHICAL CATHODE FOR LITHIUM AIR BATTERIES WITH AQUEOUS ELECTROLYTE

Ning Bi

Dr. Xing Yangchuan, Thesis Advisor

ABSTRACT

Lithium air batteries show a great promise as energy storage devices due to their high energy densities. Meanwhile, the exploiting of renewable energy sources stimulates the development of the batteries. However, currently, there are numerous scientific and technical challenges that must be addressed before commercialization. Recently, our lab has demonstrated a new hierarchical and nanostructured air cathode which shows high activity.

In this work, a new mathematical model for a hierarchical and nanostructured air cathode has been established. The model is implemented in the commercial software COMSOL and verified with the existing experimental data. Furthermore, the effects of different air cathode structure parameters have been investigated. The gas diffusion pore width plays a dual role on the cell performance and an optimal pore width has been found. The backing paper thickness has minor influence on the cell performance. Finally, the cell performance increases with the increase of the length and density of carbon nanotube assays (CNTAs) under sufficient oxygen circumstance. However, when the oxygen transport is limited, the increase of the length and density of CNTAs has no significant effect. The model developed in this work can be used as a tool to predict and optimize the structure of Li-air cathode.

Chapter 1. INTRODUCTION TO LITHIUM AIR BATTERIES

1.1. Background-factors that promote the development of Lithium air batteries

1.1.1. Grid energy storage

With the rapid growth of global population and humans' reliance on modern technology, peoples' demand for energy is increasing significantly. According to the report (Richter, D.; Greene et al. 2008), the total power consumption is currently 14 TW and is estimated to roughly triple by 2050. Among various energy resources, fossil fuels predominate. As a result, oil price volatility, global warming, local pollution, and depletion of fossil fuel resources keep reminding us to find a new way to adapt to the current fast civilization and strive to replace the traditional energy resources especially in developing countries. Unlike fossil fuels which are exhaustible, renewable energy sources, such as biomass, hydropower, geothermal, solar, wind and marine energies are naturally clean and replenishable. The renewables have received extensive attention in recent decades. According to the Annual Energy Outlook 2012 from the U.S. Energy Information Administration (EIA), renewable energy is predicted to be the fastest growing energy source (from 7% to 11%) as shown in Fig. 1.1 ((EIA) 2012). Renewable energy is expected to replace conventional fuels in different areas such as electricity generation, heating, motor fuels, and rural energy services. Among those areas, electricity generation for the electrical power grid is of great interest to scientists and engineers. It is projected that the world renewables used for electricity generation will increase from 18% in 2007 to 23% in 2035. Sunlight, especially, combined with

hydroelectricity and wind energy is expected to have the largest share in total renewable electricity generation at around 80% (Tartaglia, Fracastoro et al. 2014). Advantages of renewable energy are apparent: most of the sources are perennial and free, environmental friendly and fairly distributed in almost every country. For example, areas that are rich with running rivers or sunshine; regions which are swept by strong and regular winds; coastal areas washed by waves and so on are ideal places as renewable energy sources.

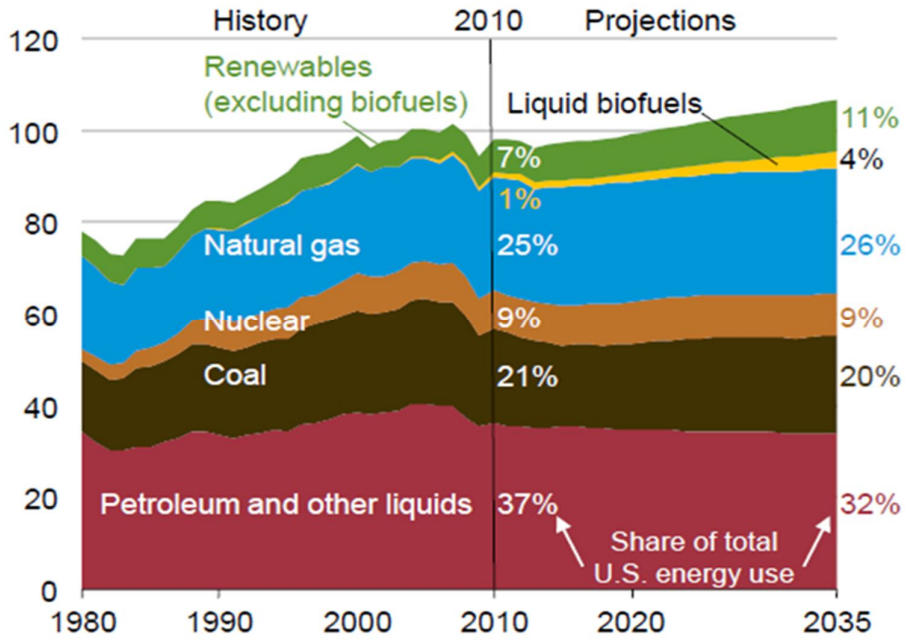

Fig. 1.1 Primary energy use by fuel, 1980-2035 (from EIA).

Although renewable energy is thought as a promising substitution to fossil fuels， and it is supported by policies from governments and innovations from laboratories and companies, there are some inherent shortcomings that hinder some of the energy sources' popularization.

I) Most renewable energy sources are diluted and diffuse. The renewable energy densities normally range from a few W/m^2 to less than 1 kW/m^2. Compared to the MW/m^2 scale of fossil fuel power plants, the renewable energy sources pale. Despite the incredible amounts of diffuse renewable energy around us such as solar radiation and wind, this type of energy is useless to us currently unless it is concentrated into forms such as electricity or fuels by facilities like solar panels or wind turbines.

II) Most renewable energy sources are intermittent and unpredictable. These two drawbacks reduce the value of the produced energy. Renewable energy sources such as solar and wind cannot render power steadily, since their power production rates vary with seasons, months, days, hours and even minutes. Thus, the electricity generated by renewable energy fluctuates.

Renewable energy sources alone cannot deliver a regular supply of energy which is easily adjustable to cater to the energy demands of the consumers. Therefore, in order for the renewable energy resources to become more reliable, energy storage is a crucial factor in the grid system. The typical smart grid system for renewable energy sources is illustrated in Fig. 1.2. The energy storage facility is usually made up of battery tanks such as Lithium air battery tanks. Along with the help of smart power management, the storage facility can store the surplus electricity generated during off-peak hours and supply stored electricity during the peak hours to meet high demand (Neetu Meena 2014).

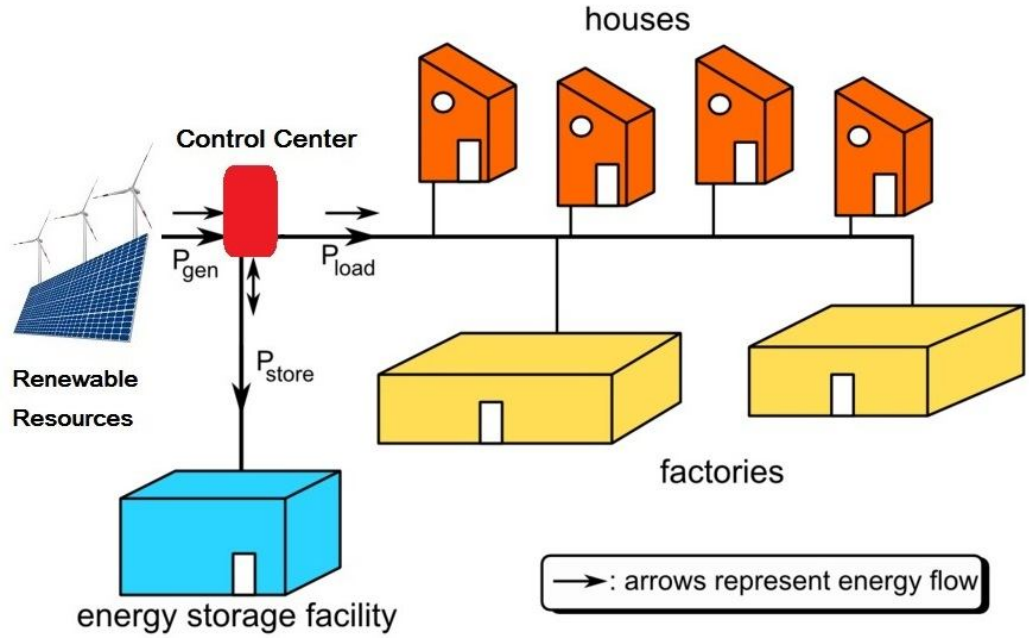

Fig. 1.2 Simplified electrical grid with energy storage (http://en.wikipedia.org/wiki/Grid_energy_storage).

1.1.2. Transportation

Environmental protection and energy issue have already become the two most outstanding themes in the new century (Hanpin Luo 2012). Almost one-third of the nation's greenhouse gas emissions come from transportation, where 60 percent is from light-duty vehicles (see Fig. 1.3). Greenhouse gas emissions from transportation mainly result from burning fossil fuel. Over 90% of the fuel used for transportation is based on petroleum consumption, which includes gasoline and diesel. Electric vehicles (EVs), ones that use electric motors for propulsion, first came into existence in the mid-19th century. The new invention was not popular until the 80's of the last century. Improvement in technologies and governments' investments provided positive conditions for the development of EVs. EVs include plug-in electric cars, hybrid

electric cars, hydrogen vehicles, etc. As a promising green traffic tool, electric vehicles were redesigned and will keep improving to solve social problems (Eberle and von Helmolt 2010).

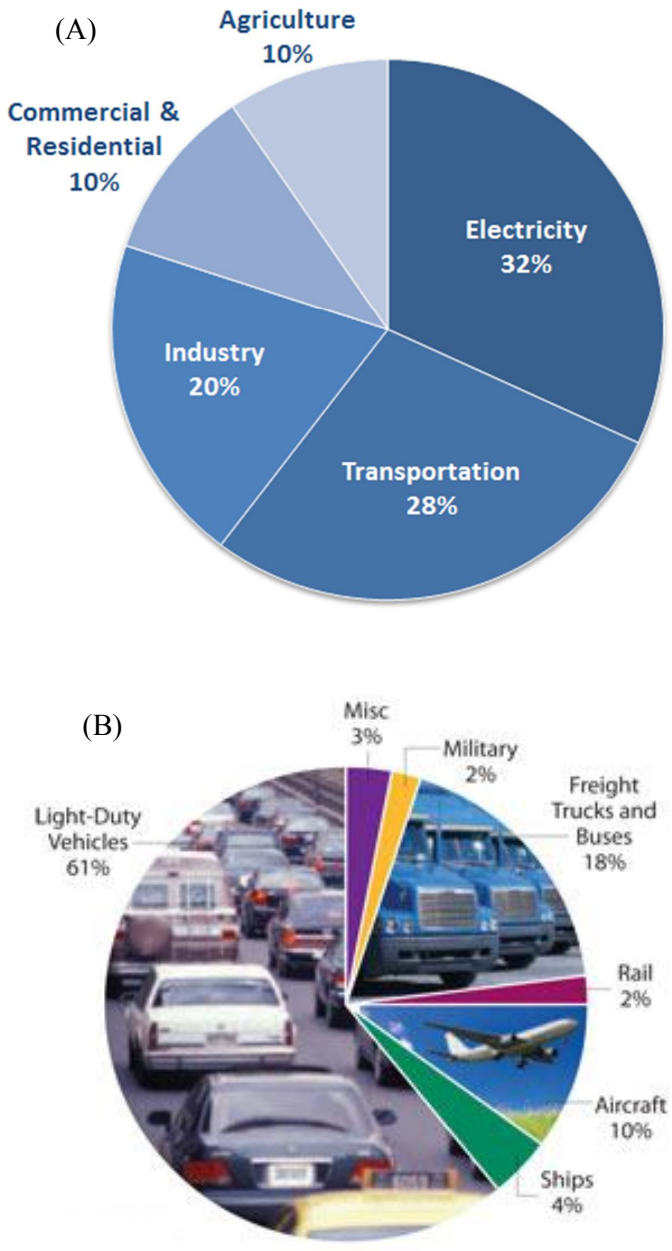

Fig. 1.3 (A) Total U.S. greenhouse gas emissions (www.epa.gov), (B) transportation emissions pie charts (www.ucsusa.org).

One of the key components in a battery electric vehicle (BEV) is the battery which is used to store energy just like the gasoline tank in a regular vehicle and provide for propulsion during the discharge process. The electric vehicle battery (EVB) can be either a primary battery or a secondary rechargeable battery. Metal-air batteries (especially the rechargeable Lithium air battery) which have high specific energy have raised the attention of scientists and engineers.

1.2. Critical review of Lithium air batteries

1.2.1. Definition of Lithium air batteries

The Lithium-air battery (Li-air battery) is a metal-air battery which generates a current flow through the oxidation of Lithium at the anode and reduction of oxygen at the cathode during the discharge process. Fig. 1.4 shows the general structure of a Li-air battery. The Li-air battery was initially proposed in the 1970s as a possible power source for automobiles to replace fossil fuels. In 1996, K.M. Abraham and co-workers published a paper demonstrating the first non-aqueous Li–air battery with the use of Lithium as the anode, a porous carbon electrode as the cathode, and a gel polymer electrolyte membrane as the separator (Jiang 1996). Since 2009, Li-air batteries have recaptured scientific interest due to advances in materials technology and the potential for replacing gasoline in EVs.

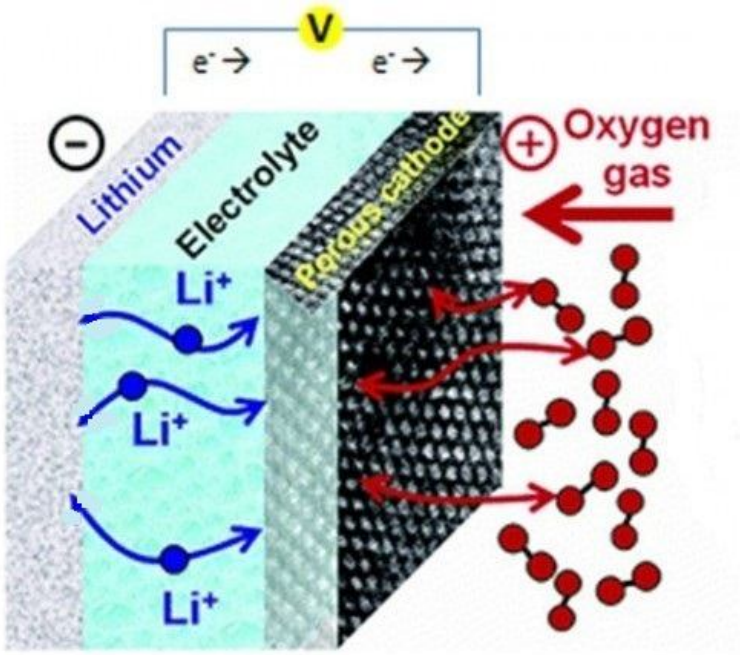

Fig. 1.4 Basic configuration of a Lithium air battery (photograph by NASA).

Before the invention of Li-air batteries, insufficient energy storage capacity of current batteries severely limited the driving range of EVs. However, Li-air batteries have theoretically much higher energy storage densities than other batteries and are comparable to that of gasoline, because the cathode active material (oxygen) is not stored in the battery, but can be accessed from the environment. The theoretical and practical energy densities of various batteries are shown in Fig. 1.5 (Girishkumar, McCloskey et al. 2010). Although Li-ion batteries are commonly used in most EVs currently, there is no expectation that Li-ion will ever come close to the future target of 1700 Wh/kg as gasoline has. The oxidation of Lithium metal could release 11680Wh/kg theoretically, which is not much lower than that of gasoline. Unfortunately, practical energy densities for Li-air batteries will be far less and need to be improved in the future (Christensen, Albertus et al. 2012, Balaish, Kraytsberg et al. 2014).

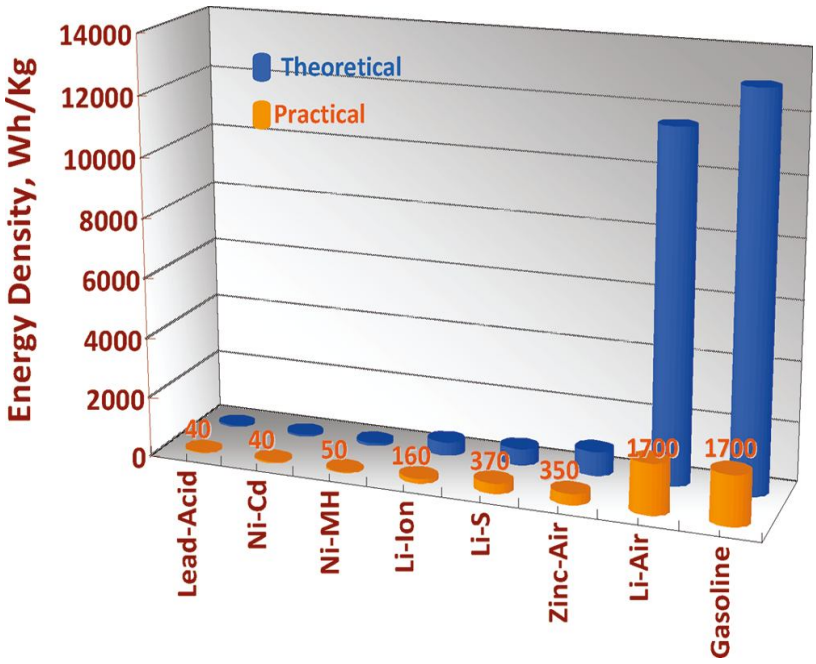

Fig. 1.5 Energy densities (Wh/kg) for various types of rechargeable batteries compared to gasoline (Girishkumar, McCloskey et al. 2010).

1.2.2. Classification of Li-air batteries

Generally, there are four kinds of Li-air batteries classified by the electrolytes used (Fig. 1.6), since the electrochemistry depends on the electrolyte used in the battery.

I) Aprotic Li-air batteries

$$2Li + O_2 \rightleftharpoons Li_2O_2 \tag{1.1}$$

and $2Li + (1/2)\ O_2 \rightleftharpoons Li_2O$ (1.2)

II) Aqueous Li-air batteries

$$2Li + 2H^+ + (1/2)O_2 \rightleftharpoons 2Li^+ + H_2O \quad \text{(Acidic media)} \tag{1.3}$$

$$2Li + H_2O + (1/2)O_2 \rightleftharpoons 2LiOH \quad \text{(Alkaline media)} \tag{1.4}$$

III) Mixed aqueous and aprotic Li-air batteries

At the anode of the batteries, the electrolyte is filled with non-aqueous liquids. While at the cathode side, aqueous electrolyte is used.

IV) Solid state Li-air batteries

The chemistry for solid state Li-air batteries is not clear yet, but is presumably the same as that for the aprotic electrolyte (Girishkumar, McCloskey et al. 2010).

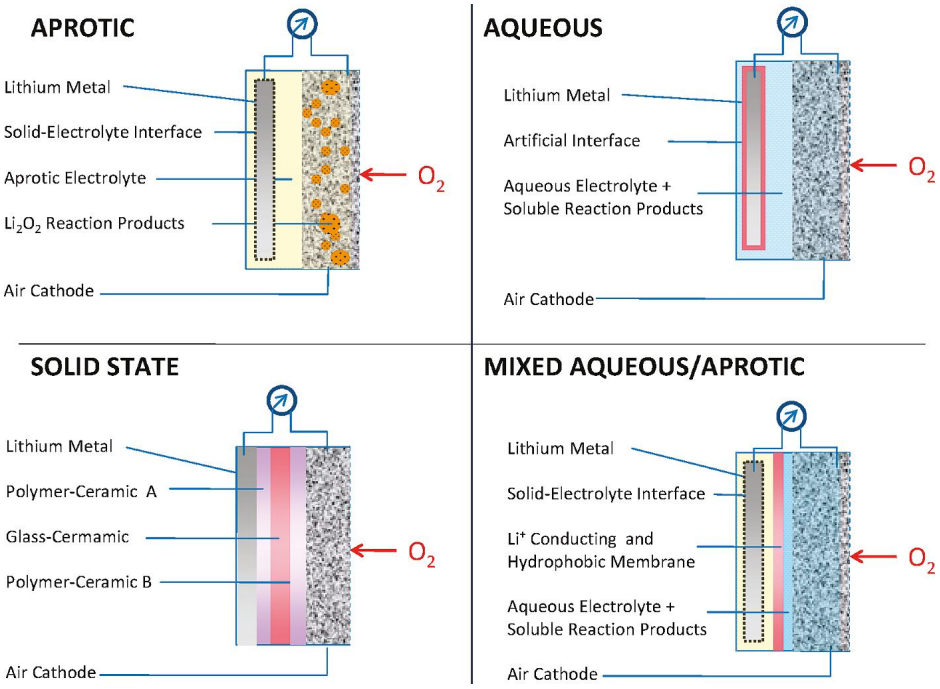

Fig. 1.6 Four different types of Li-air batteries(Girishkumar, McCloskey et al. 2010).

1.2.3. Challenges of Li-air batteries

Although the implementation of Li-air batteries holds the greatest promise in a number of applications ranging from grid energy storage to electric vehicles, there are also a lot of significant challenges in the development of future Li-air batteries (Kraytsberg and Ein-Eli 2011).

Hurdles are exist in different types of Li-air batteries, for example:

I) Truly reversible electrochemical reactions need to be established. Side reactions may impede the efficiency and cycle life of the batteries (B. McCloskey 2011, G. M. Veith 2011, S. A. Freunberger 2011, W. Xu 2011).

II) Stabilizing the Li metal negative electrode (except solid state electrolyte). Since Lithium is an active material, how to prevent Lithium from reacting with the electrolyte is important.

III) Supplying contaminant-free O_2 to the system. Other components of air may participate as side reactions during the discharging process.

1.3. Motivations and objectives for this research

The Li-air battery research projects in Xing's lab are mainly focused on aqueous Li-air batteries rather than non-aqueous ones, because the products in aqueous media are significantly more soluble in water (Li, Huang et al. 2012, Li, Huang et al. 2013). Li-air battery performance limitations are largely related to the air cathode including the electrolyte, structure, operation temperature, etc., resulting from the fact that the cathode reaction delivers the largest part of the cell energy, and most of the cell voltage

drop occurs at the air cathode. Therefore, one of the main and critical tasks in our lab is to find a suitable cathode for aqueous Li-air batteries.

Recently, Dr. Xing and coworkers have successfully prepared a nanostructured, hierarchical cathode consisting of Nitrogen doped (N-doped) carbon nanotube arrays (CNTA) and a backing carbon paper (Li, Huang et al. 2013). Sparsely populated, vertically aligned, and straight CNTAs are grown on carbon fibers by plasma enhanced chemical vapor deposition method, resulting in a highly porous and active cathode for reactions (see Fig. 1.7). Utilization of straight and sparsely distributed N-doped carbon nanotubes arrays is advantageous. First, they are more resistant to electrochemical corrosion than conventional porous carbon black. Second, they provide significantly abundant catalytically active sites for Li-air batteries with alkaline electrolytes. Finally, highly porous CNTAs helps the transport of oxygen.

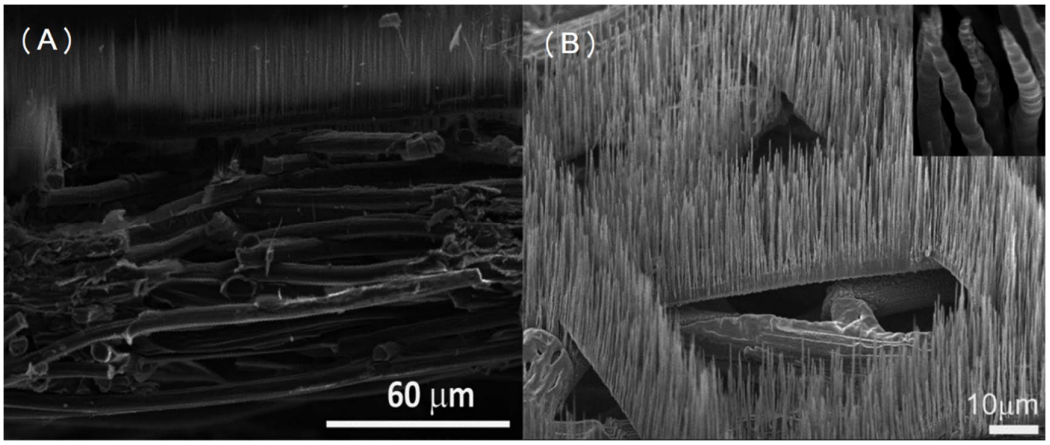

Fig. 1.7 SEM images of CNTAs gown on a backing carbon paper (A) cross-sectional view, (B) CNTAs with a site density of ~10^7 cm^{-2}(Li, Huang et al. 2013).

The cathode is filled with 0.5 M LiOH and 0.5 M $LiNO_3$ and then assembled with a protected metallic Li anode. The reversible electrode reaction chemistry is as follows:

$$\text{Anode:} \quad Li \rightleftharpoons Li^{+} + e^{-} \tag{1.5}$$

$$\text{Cathode:} \quad 1/4O_2 + 1/2H_2O + e^{-} \rightleftharpoons OH^{-} \tag{1.6}$$

The reactive sites are the surface defects on the CNTAs as a result of the expanded N-doped graphite layer edges. Oxygen reduction reaction (ORR) takes place on those sites. The reaction mechanism is illustrated in Fig. 1.8

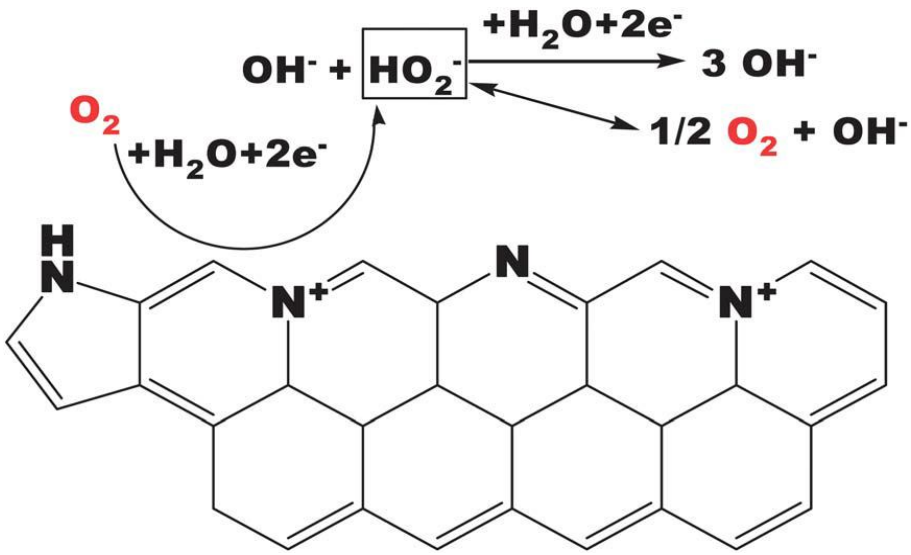

Fig. 1.8 ORR mechanisms on N-doped CNTs (Li, Huang et al. 2013).

In light of the lab's recent study, the cathode structure is a key factor that impacts the overall performance of the batteries. In order to evaluate the effect of various structure parameters, a modeling method is used in this work to predict the effects and the optimum parameters. The benefit of establishing a model is that if a suitable model is

built, one can reduce the experiments that need to be done to save materials and time. Moreover, there are few papers that have modeled the Li-air battery with aqueous electrolyte, not to mention the nanostructured cathode. The object of this research is to, for the first time, establish a hierarchical and nanostructured cathode model. After the model is validated, the effects of different structural parameters can be studied in order to find the optimum structure.

Chapter 2. MATHEMATICAL MODELS

2.1. Cathode Structure

The schematic diagram of a cathode is shown in Fig. 2.1 and Fig. 2.2. It combines the vertically oriented CNTAs as a catalyst layer and a porous carbon fiber paper as a backing layer to grow CNTAs. From experiment, CNTAs are only grown on the surface of the bottommost carbon fibers. The CNTAs consist of N-doped CNTs which accelerate the ORR at the defects (reaction sites) of the CNTs. The catalyst layer is fully flooded with alkaline solution (Li, Huang et al. 2013).

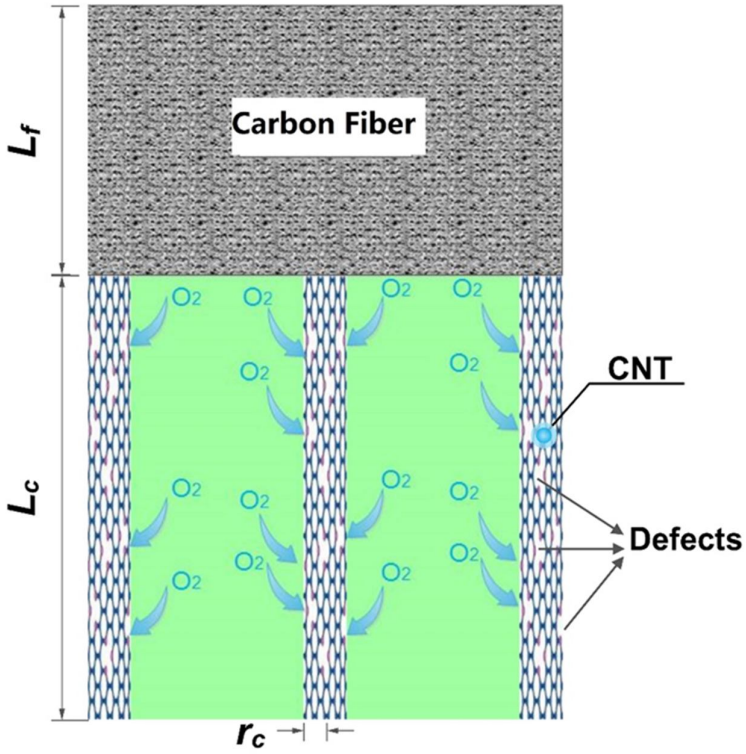

Fig. 2.1 Enlarged side view of nanostructured cathode of Lithium air battery with backing carbon paper and vertically aligned CNTAs.

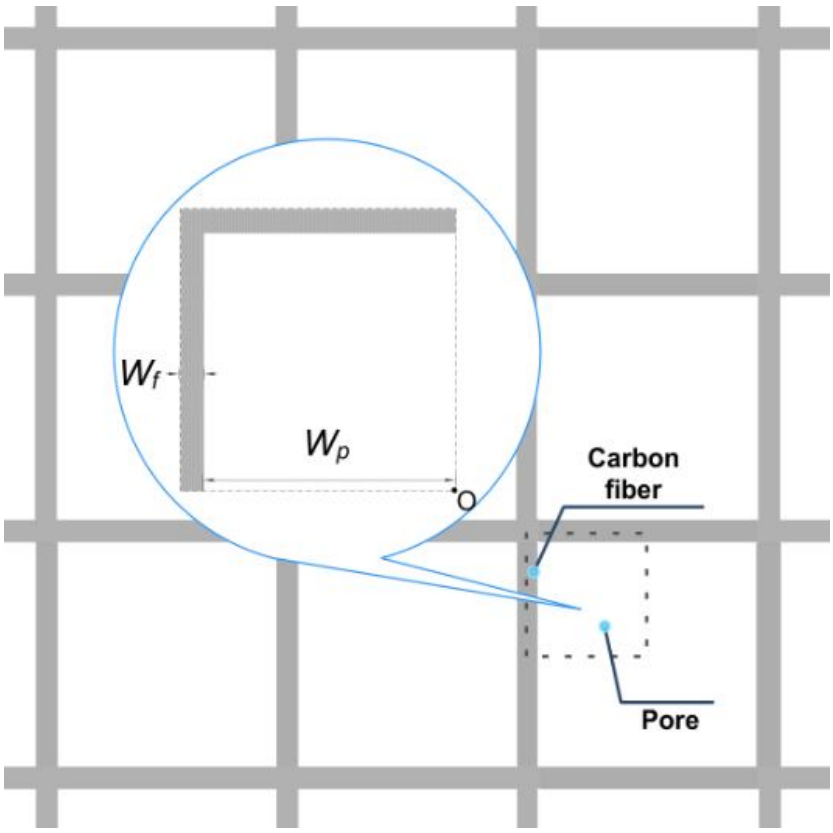

Fig. 2.2 Top view of the cathode structure.

The whole process can be briefly described as the external air diffusing into the pores of the backing layer. At the boundary of the backing layer and catalyst layer, only oxygen is dissolved into the electrolyte. After that, oxygen is partially or fully consumed upon arrival at the external surface defects of the CNTAs on the carbon fibers.

2.2. Assumptions

In this study, for simplification purposes, we assume that the carbon fibers are evenly distributed along with the straight square pores to form a net shape. Thus from Fig. 2.2,

we choose a square area as our modeling domain for simplicity because of symmetry. Fig. 2.3 depicts the 3D schematic diagram of the proposed computational domain. There are four subdomains in the simulation: carbon fiber domain, gas diffusion pore domain, electrolyte domain, and reaction domain (made up of CNTAs and electrolyte).

We assume that oxygen cannot penetrate the fibers. The electrolyte is evenly distributed. Also, for modeling simplification, we assume that the CNTAs are the same and uniformly distributed on the fibers as well as the defects at the surface of the CNTAs. Therefore, homogeneous reaction in the reaction domain is assumed.

There is no convection in the cathode, so diffusion dominates the transport of oxygen. There is a sufficient amount of water and hydroxides in the electrolyte, which means that the only limiting factor is the oxygen concentration. We could neglect the ion transport in the electrolyte. The cell is operated under steady state and isothermal conditions. Moreover, we assume that the overpotential is constant along the length of the CNTAs.

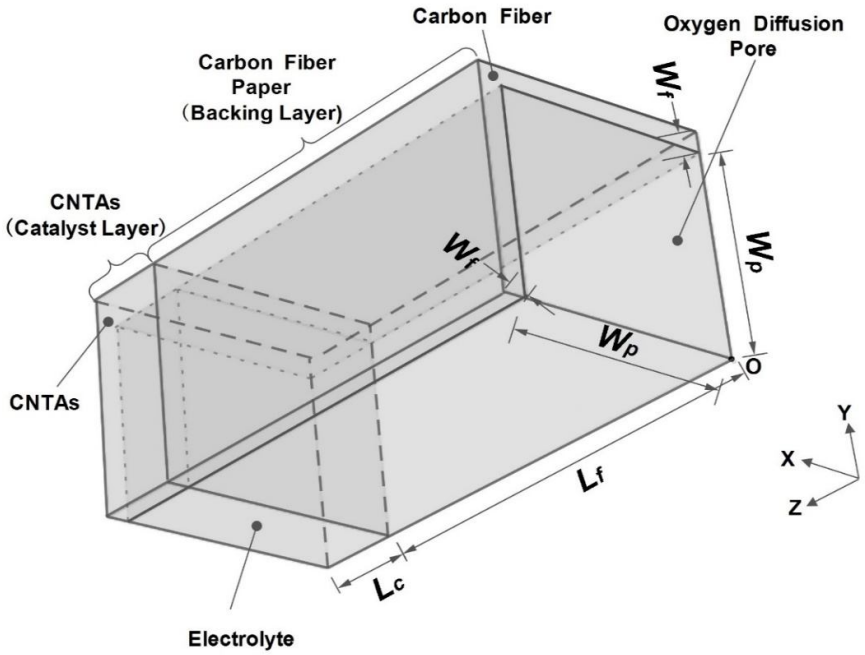

Fig. 2.3 Axisymmetric scheme of simulated domain.

2.3. Governing equations

2.3.1. Oxygen Transport through pores of the backing layer

The air which is mainly a mixture of oxygen and nitrogen diffuses through the straight pores of the backing layer and finally reaches the boundary of the catalyst layer. The oxygen transportation equation is approximated by the Fick's law of diffusion (R.B. Bird 2007) which gives

$$\nabla \cdot \left(-D_{O_2\_g} \nabla c_{O_2\_g} \right) = 0 \tag{2.1}$$

Where $D_{O_2\_g}$ and $c_{O_2\_g}$ are the oxygen diffusion coefficient and the oxygen concentration in the pores of the backing layer.

2.3.2. Oxygen Transport in the catalyst layer

Since only oxygen can be dissolved into the electrolyte, the diffusion of oxygen is also modeled by the Fick's law of diffusion in the electrolyte domain and in the reaction domain, respectively.

$$\nabla \cdot \left(-D_{O_2\_l} \nabla c_{O_2\_l} \right) = 0 \tag{2.2}$$

$$\nabla \cdot \left(-D_{O_2\_l} \nabla c_{O_2\_l} \right) = -R_{orr} \tag{2.3}$$

Where $D_{O_2\_l}$ and $c_{O_2\_l}$ are the oxygen diffusion coefficient and the oxygen concentration in the electrolyte within the catalyst layer. R_{orr} is the reaction rate of the oxygen reduction rate (ORR).

2.3.3. Boundary conditions

In order to solve the above equations, the boundary conditions applied for all the boundaries shown in Fig. 2.3 are as follows

(1) Backing layer

In the backing layer, the simulated domain is the pore for oxygen diffusion. At $Z = 0$, the inlet concentration of oxygen is specified. At $Z = L_f$, the oxygen concentration is solved from the governing equations. At $Y = 0$ and face $X = 0$, the flux is set to be zero which means that the symmetric boundary condition is applied, resulting from the fact that these areas are symmetric to their adjacent parts because of the symmetric geometry. At the boundaries of pores and fibers which are $Y = W_p$ and $X = W_p$, the insulation boundary condition is applied, because oxygen cannot permeate the fiber as we assumed before.

(2) Catalyst layer

Oxygen diffuses in the electrolyte of the catalyst layer and only reacts in the reaction area. At $Z = L_f$, there are two parts of boundaries. At the bottom face of the pore (i.e. the interface of the electrolyte and pore), the amount of oxygen that dissolves from the gas phase in the electrolyte is calculated by the Henry's law (D.M. Bernardi 1991, D.M. Bernardi 1992)which is shown in Eq. 2.4

$$c_{O_2\_l} = K_{O_2} c_{O_2\_g} \tag{2.4}$$

At the bottom face of the fiber, the insulation boundary condition is used to describe the oxygen transport behavior. At $Z = L_f + L_c$, the flux of oxygen is zero. At $X = 0$, $Y = 0$, $X = W_p + W_f$, and $Y = W_p + W_f$ the symmetric boundary condition is applied. The continuous boundary condition is utilized at $X = W_p$ and $Y = W_p$.

2.3.4. Initial conditions

We assume that oxygen is initially uniform. Initial values are listed in the parameter table 2.1.

2.3.5. Oxygen reduction reaction

The oxygen reduction reaction is sluggish which results in a large kinetic overpotential. Moreover, we only consider the discharge situation. Thus, the Butler-Volmer's equation (A.J. Bard 2001) (Eq. 2.5) can be simplified to Tafel's equation (John Newman 2004) (Eq. 3.6) to describe the oxygen reduction reaction.

$$R_{orr} = k_c c_O \exp\left(-\frac{\alpha_c F}{RT}\eta_s\right) - k_a c_R \exp\left(\frac{\alpha_a F}{RT}\eta_s\right) \tag{2.5}$$

$$R_{orr} = k_{orr}\left(\frac{c_{O_2\_l}}{c_{O_2\_l\_ref}}\right)\exp\left(-\frac{\alpha_c F}{RT}\eta_s\right) \tag{2.6}$$

where k_c and k_a are rate constants for the cathodic and anodic reaction direction respectively, c_O and c_R are concentration of reactants, α_c and α_a are called apparent transfer coefficients which are determined by experiments, and F is the Faraday's constant. R is the gas constant, T the cell operation temperature, $c_{O_2\_l}$ the concentration in the electrolyte, $c_{O_2\_l\_ref}$ the reference oxygen concentration in the electrolyte which equates the initial concentration, and η_s the surface overpotential which is determined by the equation below (Rao and Xing 2008)

$$\eta_s = \Phi_{solid} - \Phi_{electrolyte} - U_0 \tag{2.7}$$

Φ_{solid} and $\Phi_{electrolyte}$ are the local phase potentials, U_0 the equilibrium potential (thermodynamic open circuit voltage) with the value of 3.44V in the simulation, and k_{orr} the ORR rate constant which is expressed by:

$$k_{orr} = \frac{d_{CNTAs} A_c d_{defects} R_{site}}{L_c} \tag{2.8}$$

where d_{CNTAs} is the density of the CNTAs, $d_{defects}$ the defects density on the CNT, R_{site} the reaction rate on one site, L_c the length of the CNT, and A_c the surface area per CNT which is calculated by

$$A_c = 2\pi r_c L_c \tag{2.9}$$

where r_c is the radius of the CNT.

2.3.6. Total current in the reaction domain

The total current in the reaction domain can be calculated by integrating the ORR rate over the whole domain as described below (Li and Faghri 2012)

$$I_{\text{total}} = nF \int R_{orr} dxdydz \tag{2.10}$$

where I_{total} is the total current in the simulated reaction domain and n is the number of electrons transferred.

2.3.7. Cell potential

The cell potential is calculated by

$$V_{cell} = U_0 - \eta_s \tag{2.11}$$

2.3.8. Current density

The current density is calculated by

$$I_d = \frac{I_{total}}{(W_p + W_f)^2} \tag{2.12}$$

2.4. General nomenclature and parameters

Since the accuracy of the model strongly depends on the measurement method of the model dependent parameters, particular attention was paid to carefully determining the model parameters by using existing data from our lab and those published in the literature.

Table 2.1 General nomenclature and parameters

Parameter	Value	Units	References
Temperature, T	298.15	K	(Li, Huang et al. 2013)
Pressure, p	101325	Pa	(Li, Huang et al. 2013)
Faraday's constant, F	96487	C mol^{-1}	
Gas constant, R	8.314	J mol^{-1} K^{-1}	
CNT radius, r_c	5×10^{-8}	m	(Li, Huang et al. 2013)
Diffusivity of O_2 in backing layer, $D_{O_2\_g}$	1.89×10^{-5}	m^2 s^{-1}	(Mason)
Diffusivity of O_2 in catalyst layer, $D_{O_2\_l}$	1.75×10^{-9}	m^2 s^{-1}	(M. K. Tham 1970)

Henry's constant, K_{O_2}	0.05133		(Mason)
reference oxygen concentration in electrolyte, $c_{O_2\_l\_ref}$	0.43997	mol m^{-3}	calculated from (Mason)
Length of CNTAs, L_c	*[1]	m	
Thickness of carbon paper, L_f	*	m	
Half width of the carbon fiber, W_f	5×10^{-6}	m	(Li, Huang et al. 2013)
Half width of the gas diffusion pore, W_p	*	m	
Surface area of single CNT, A_c	Eq. 2.9	m^2	
Defects density on one CNT, $d_{defects}$	7×10^{15}	m^{-2}	assumed
Density of the CNTAs, d_{CNTAs}	*	m^{-2}	
Reaction rate of one site, R_{site}	3.07×10^{-23}	mol s^{-1}	
ORR rate constant, k_{orr}	Eq. 2.8	mol m^{-3} s^{-1}	
Surface overpotential, η_s	Eq. 2.7	V	
Oxygen initial concentration in the backing layer, $c_{O_2\_g\_o}$	8.5714	mol m^{-3}	calculated
Oxygen initial concentration in the catalyst layer, $c_{O_2\_l\_o}$	0.43997	mol m^{-3}	(Elliot, Chenier et al. 1990)
Total current, I_{total}	Eq. 2.10	A	
Reaction rate of the ORR, R_{orr}	Eq. 2.6	mol m^{-3} s^{-1}	
Oxygen concentration in the gas diffusion pore domain, $c_{O_2\_g}$		mol m^{-3}	
Oxygen concentration in the catalyst layer, $c_{O_2\_l}$		mol m^{-3}	
Apparent anodic transfer coefficients, α_a	0.2		assumed
Rate constants for the cathodic reaction, k_c		s^{-1}	
Rate constants for the anodic reaction, k_a		s^{-1}	
Concentration of oxidized reactants, c_O		mol m^{-3}	
Concentration of reduced reactants, c_R		mol m^{-3}	
Local solid phase potential, Φ_{solid}		V	

[1] '*' Value varies with structure

Local liquid phase potential, $\Phi_{electrolyte}$		V	
Equilibrium potential, U_0	3.44	V	(Li, Huang et al. 2013)
Number of electrons transferred, n	4		(Li, Huang et al. 2013)
Current density, I_d		mA cm^{-2}	

2.5. Numerical implementation

The mathematical model including governing equations and boundary conditions is simulated using COMSOL Multiphysics. A finite element method with a nonlinear solver is used by the software to solve the differential equations over the 3D geometry. Extra fine mesh parameters are utilized to discretize the target domains into elements and then implement a non-linear solver. A parametric sweep method is used.

Chapter 3. RESULTS AND DISCUSSIONS

3.1. Model Validation

In order to justify the rationality and accuracy of the model, the modeling results are compared with the experimental data reported by our laboratory in the literature. We treat the corresponding model, which is similar to cell structure and operation condition in the literature, as the base case in our model. The parameters selected in the validation of the proposed model (i.e. base case) are listed in both Table 3.1 and Table 2.1.

Table 3.1 Base case specific parameters for model validation

Parameter	Value	Units	References
Length of CNT, L_c	2×10^{-5}	m	(Li, Huang et al. 2013)
Depth of carbon fiber, L_f	1×10^{-4}	m	(Li, Huang et al. 2013)
Half width of the gas diffusion pore, W_p	5×10^{-5}	m	(Li, Huang et al. 2013)
Density of the CNTAs, d_{CNTAs}	10^{10}	m^{-2}	(Li, Huang et al. 2013)
Surface area of single CNT, A_c	6.283×10^{-12}	m^2	assumed
ORR rate constant, k_{orr}	0.0675	mol m^{-3} s^{-1}	calculated

After the model carries out a parametric sweep, the cell voltage vs. current density are computed under various discharge current density values. Fig. 3.1 shows the comparison between the model predicted data and the experimental data of the cell performance. The X-axis represents the current density and the Y-axis represents the cell potential. The variable current density rather than the regional total current renders a better aspect of the overall cell performance, because current density is the average current in the whole catalyst layer. The solid line represents the model predictions, while the dashed line indicates the experimentally measured data obtained in our

laboratory. It is shown from the figure that as the current density increases, the cell potential drops. The simulated cell performance exhibits a similar tendency as the experiment data throughout the current density range. Errors lie within 0-0.15 V. Hence, the modeling results are in good agreement with the measured data (Li, Huang et al. 2013). It should be noted that because of the ideal assumption that the internal impedance is neglected, the modeling result tends to reach a plateau at larger current density within the simulated current density region.

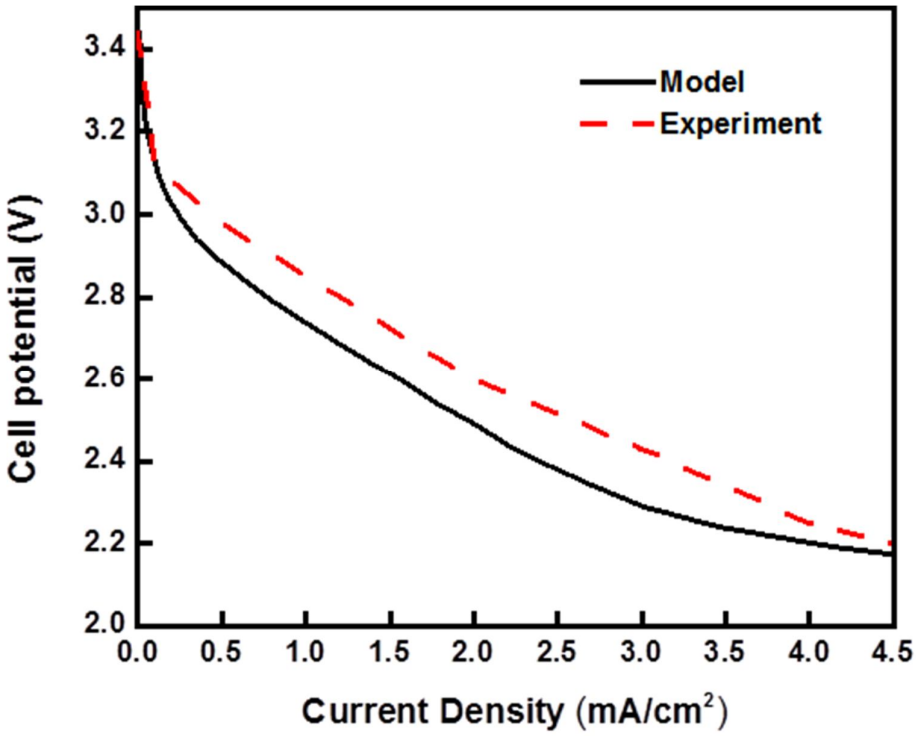

Fig. 3.1 Comparison between modeling results and experimental data of current density vs. voltage.

Another way to verify the reliability of the model is by checking the oxygen concentration distributions from the modeling results. Fig. 3.2 and Fig. 3.3 show 3D oxygen concentration distributions in both the catalyst layer and the backing layer when

applied current density equates to 2mA/cm^2. The oxygen concentration change in the backing layer is quite small, while it is more significant in the catalyst layer resulting from the large differences between diffusion coefficients. The diffusivity of oxygen in the liquid phase is four orders of magnitude lower than that in the gas phase. Because of the symmetry property of the simulated domain, there is a symmetry diagonal plane in the domain. The oxygen is consumed much faster near the corner of the pore than other places, since the reaction sites are regionally more concentrated at that area, because oxygen diffusion rate is limited by the diffusivity. Hence, when Z increases, the oxygen concentration drops.

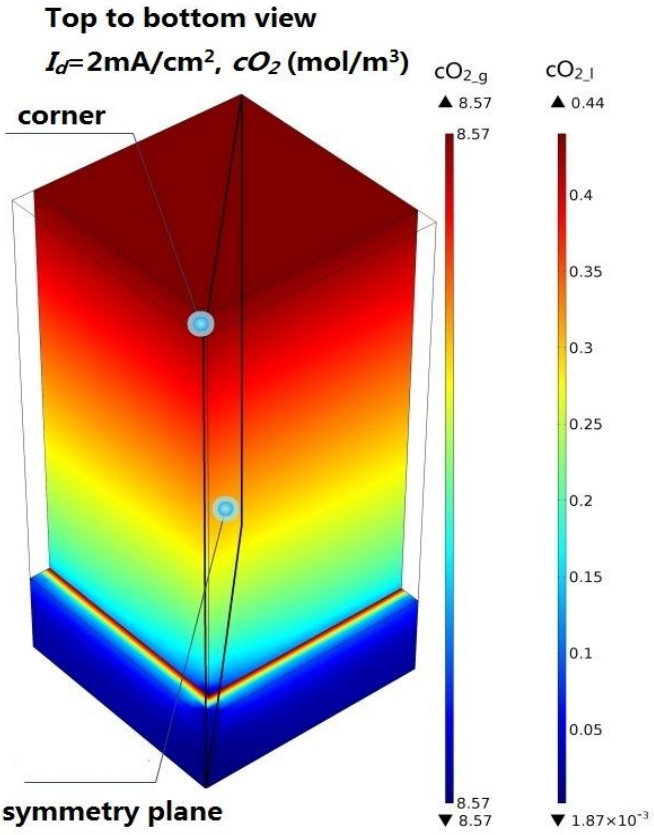

Fig. 3.2 Top to bottom view of the oxygen concentration distributions in simulated domain.

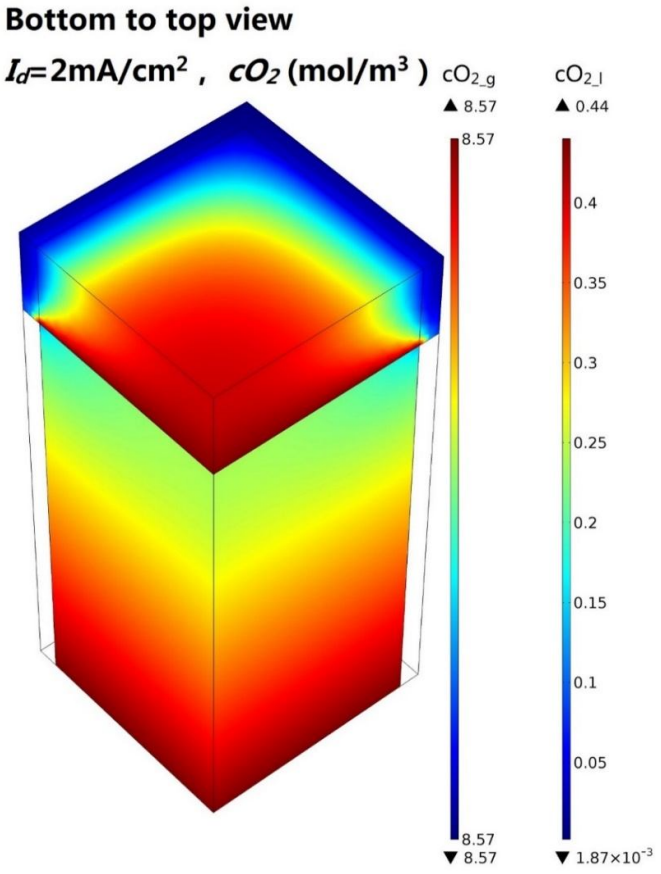

Fig. 3.3 Bottom to top view of the oxygen concentration distributions in simulated domain.

We can also test the validity of the model by changing current densities and looking into how the oxygen distribution changes at the same places. If we cut a cross sectional plane right in the middle of the catalyst layer (i.e. at $Z = L_f + L_c / 2$), there will be an x-y directional slice. For simplicity purposes, we only look at this slice. Fig. 3.4 shows Oxygen concentration distribution vs. current densities under four operating values. As the current density increases, the oxygen concentration decreases correspondingly. It is reasonable because larger current density means more reaction when pore size is fixed,

followed by the increased consumption of dissolved oxygen, which in turn decreases the dissolved concentration of oxygen in the electrolyte. Thus, oxygen will be utilized more when current density increases. In conclusion, from these points of view, this model is valid within the current density range i.e. from 0 to 4.5mA/cm^2. In the following sections, all the current density ranges are kept in the validated range in this section.

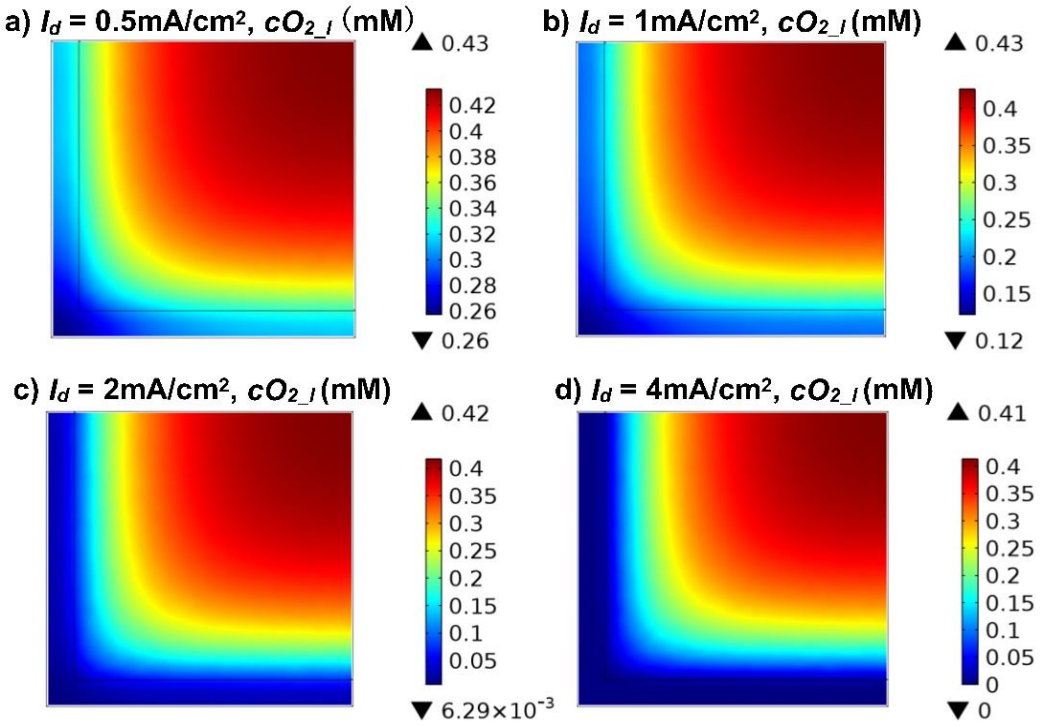

Fig. 3.4 Oxygen concentration change under different current densities

3.2. The effects of cathode structure on the performance of the cell

This model helps obtain the performance of the cathode that is operated under various conditions as well as the concentration distributions of oxygen in different phases.

Through the variation of the structure parameters, optimal selection of the structure can significantly increase the performance of the cell.

3.2.1. Effects of gas diffusion pore width (W_p) in the backing layer

(1) Effects of the pore width on the performance of the cell

In order to study how gas diffusion pore width influences the performance of the cell, pore width is the only parameter changed in the simulation, while all other parameters are kept the same to the base case. Pore widths of 20μm, 50μm, 100μm, 200μm sizes are chosen respectively.

Table 3.2 W_p values for different gas diffusion pore sizes

Case Number	W_p (m)
1	1.25×10^{-5}
2	2.5×10^{-5}
3	5×10^{-5}
4	10×10^{-5}

Fig. 3.5 depicts the effect of gas diffusion pore width in the backing layer on the performance of the cell. The applied current density sweeps from 0 to 4.5mA/cm^2 to predict the corresponding cell potential. Fig. 3.5 presents that under the same overpotential; current density is relatively larger in the smaller pore width cases which means better performance. This phenomena is due to the fact that the number of reaction sites per unit geometrical area increases along with the decrease of pore width, since the carbon fiber width is kept as a constant. In a given area, when oxygen supply is sufficient, more reaction sites can render better performance. It can be concluded from this figure that the reaction sites per unit area plays a dominating role in cell performance when the pore with is larger than 20μm. Hence, decreasing the pore width will improve the overall cell performance at this pore width range.

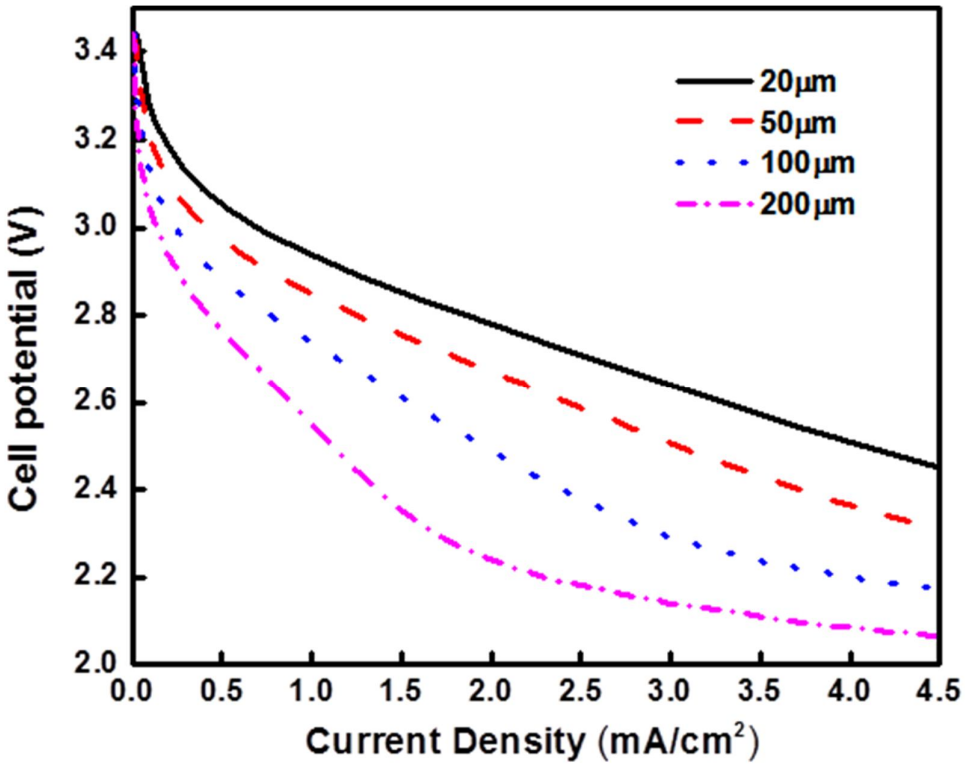

Fig. 3.5 Effect of the gas diffusion pore width ($2W_p$) on the performance of the cell at larger pore width.

However, from the previous experiment in our laboratory, oxygen diffusion efficiency will be hindered by reducing the pore size leading to worse ORR. Because larger spacing renders more space for oxygen diffusion in the electrolyte and subsequently more efficient ORR. It is supported by the oxygen concentration distribution diagrams from the simulation (see Fig. 3.6): We still look into the slice at $Z = L_f + L_c / 2$. This time, a constant overpotential of 0.7 Volts is applied in each case to help study the oxygen distribution, since fixed overpotential gives us constant reaction rates everywhere if oxygen is supplied sufficiently according to Eq. 2.6. It is clear from Fig. 3.6 that a higher oxygen concentration covers more area in larger pores. Thus, reducing

pore width can cause worse oxygen transport efficiency resulting in worse ORR rate and worse cell performance because of the decrease in oxygen concentrations. This result looks contradictory with the conclusion from Fig. 3.5. We speculate that when pore width is larger than 20μm oxygen transport limitation is not significant enough when compared with the factor of reaction sites per unit area. However, if the pore width continues to decrease below 20 μm, the oxygen diffusion limitation may start to play a leading role in the cell performance rather than the reaction sites per unit geometrical area.

Another pore width range from 5 μm to 20 μm was studied. The results from Fig. 3.7 confirm our conjecture. Fig. 3.7 shows that at higher cell potential region (i.e. , $V_{\text{cell}} \geq 2.92\text{V}$) where the ORR rate is small, reducing the pore width will increase the current density because the oxygen consumption is not very fast and oxygen supply is sufficient which means that the number reaction sites plays a dominant role. However at lower cell potentials (i.e. $V_{\text{cell}} \leq 2.92\text{V}$), where the ORR rate is fast, reducing the pore width will first undergoes a current density increment and then the current density keeps decreasing. The decrease is the result of the oxygen transport limitation that plays a dominant role. We can conclude from the analysis above that, when oxygen supply is sufficient, decreasing pore width helps the increase of cell performance, since reaction sites per unit geometry area is the major factor to consider. When oxygen supply is insufficient, decreasing pore width will further hinder the transport of the oxygen resulting in the poor cell performance. Considering both factors above, there should be an optimum width for the cell. Optimization methods will be discussed in the next section.

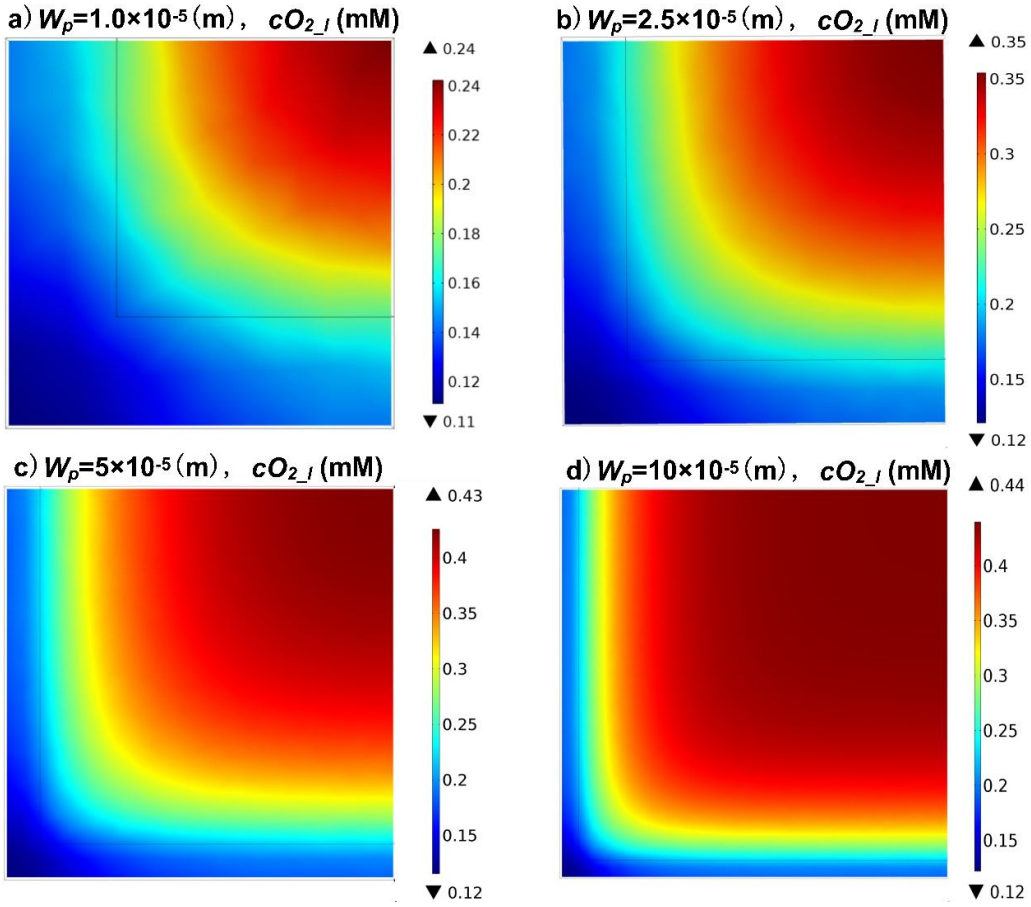

Fig. 3.6 The effect of pore width ($2W_p$) on the oxygen concentration distribution under constant overpotential of 0.7V.

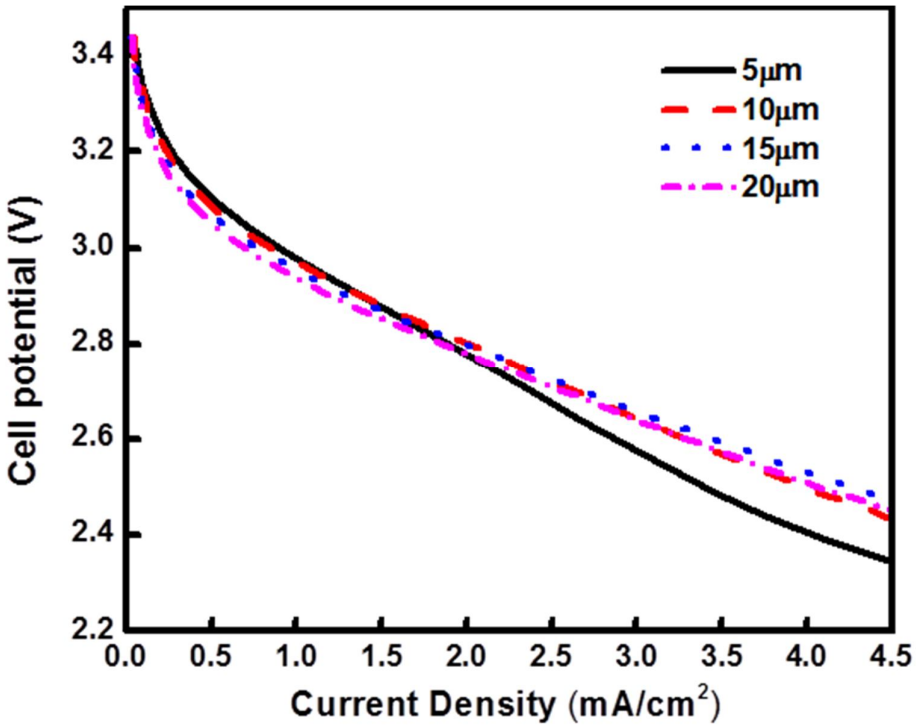

Fig. 3.7 Effect of the gas diffusion pore width ($2W_p$) on the performance of the cell at smaller pore width.

(2) Optimization of the pore width

As mentioned above, oxygen transport is considered to be one of the key factors to improve the Lithium air battery performance, because it affects the catalyst efficiency. If there is an insufficient oxygen supply situation, which means that oxygen cannot reach all the surface reaction sites (especially at higher current densities) due to low diffusivity, non-uniform utilization of the electrode resulting in a wastage of cathode material and decrease of specific energy. Thus, a sensible way of designing the structure of a catalyst layer would be to optimize the pore width. Depending on the cell operation potential and the corresponding current density, the optimal pore width may differ under

different cases. An example of this optimization approach is illustrated in Fig. 3.8. We suppose that the cell is operated under the 2.89V according to Li's paper (Li, Huang et al. 2013). Fig. 3.8 shows that when the pore width increases from 2μm to 10μm, the cell current density increases and reaches the highest point. However, after that, continuing width increment leads to the drop of the cell performance. We can conclude that under 2.89V operating situation, the best pore width would be 10μm, which will be called the optimized pore width case (OPWC).

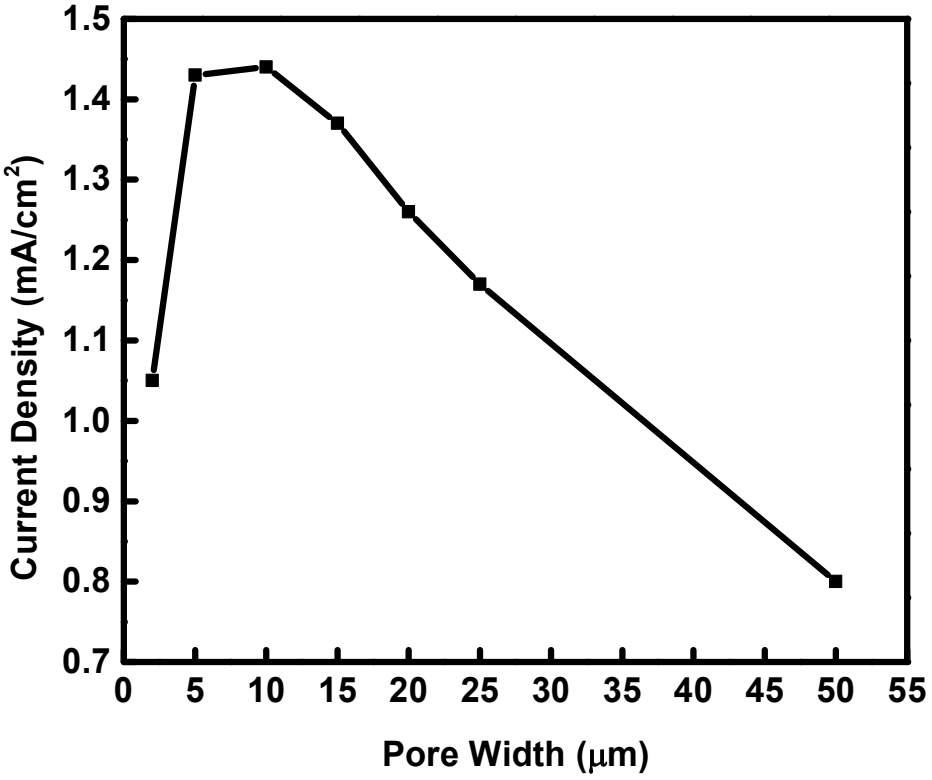

Fig. 3.8 Optimal pore width ($2W_p$) for the cell running under 2.89 V condition.

3.2.2. Effect of backing layer thickness (L_f)

Several backing layer thicknesses (100μm, 200μm, 400μm, 800μm) are used in the established model. Again, all the other structural parameters are kept the same with the base case.

Table 3.3 Four cases with different backing layer thickness

Case Number	L_f (m)
1	1×10^{-4}
2	2×10^{-4}
3	4×10^{-4}
4	8×10^{-4}

From Fig. 3.9, it is clear that the increase of the carbon paper thickness will almost have no influence on the cell at a lower current density (i.e. from 0 to 1.5 mA/cm^2). Because of the large oxygen mass transfer rate in the backing paper layer together with the micro level size of pores, the oxygen can be supplied sufficiently and efficiently at lower current densities. Thus, the cell performances of the four cases are almost the same to each other at that range. However, under the larger applied current density (i.e. from 1.5 to 4.5 mA/cm^2) region, the thickness of the carbon paper in the backing layer will gradually influence the performance of the cell. This is because at larger current densities, oxygen is consumed more rapidly, giving rise to the shortage of oxygen in the reaction domain, especially at the bottom area of the CNTAs. Therefore, it is better to reduce the thickness of the backing layer, especially when the cell is operated under large current density conditions.

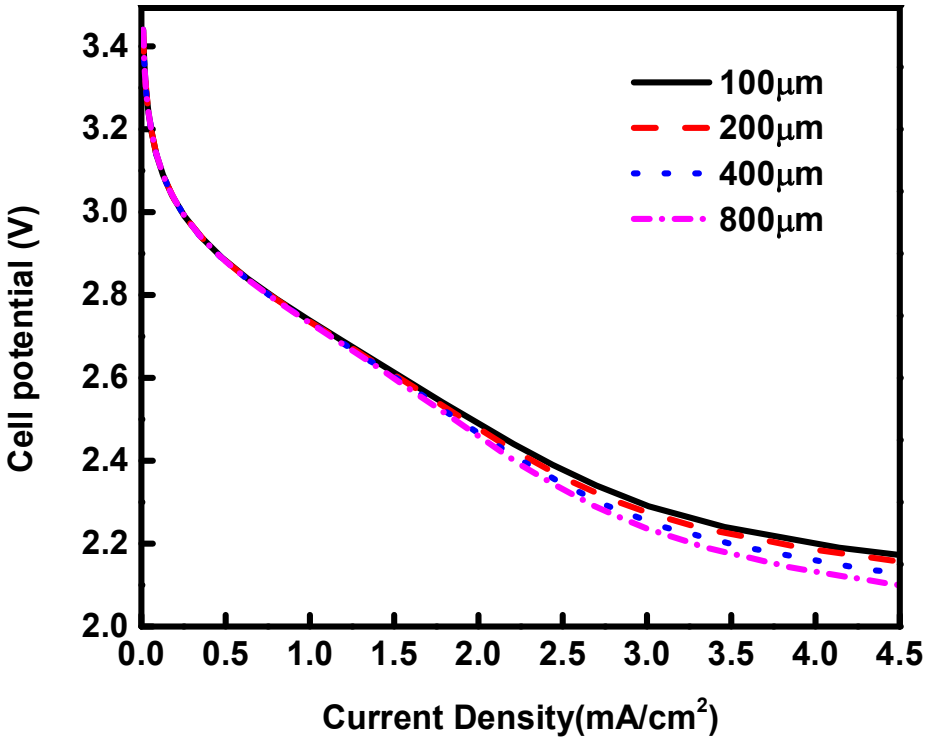

Fig. 3.9 The effect of backing paper thickness (L_f) on the performance of the cell.

3.2.3. Effect of CNTAs length (L_C)

The CNTAs lengths are selected at 5μm, 10μm, 20μm, and 40μm, while the remaining structural parameters are kept the same with the base case.

Table 3.4 L_c values for CNTAs length effect study

Case Number	L_c (m)
1	5×10^{-6}
2	10×10^{-6}
3	20×10^{-6}
4	40×10^{-6}

From Fig. 3.10, as the length of CNTAs increases, the current density increases as well when the cell potential is fixed, which means that the performance of the cell improves

as well. This is because longer CNTAs offers more reaction sites to consume oxygen. Thus, increasing the CNTAs' length can lead to better cell performance.

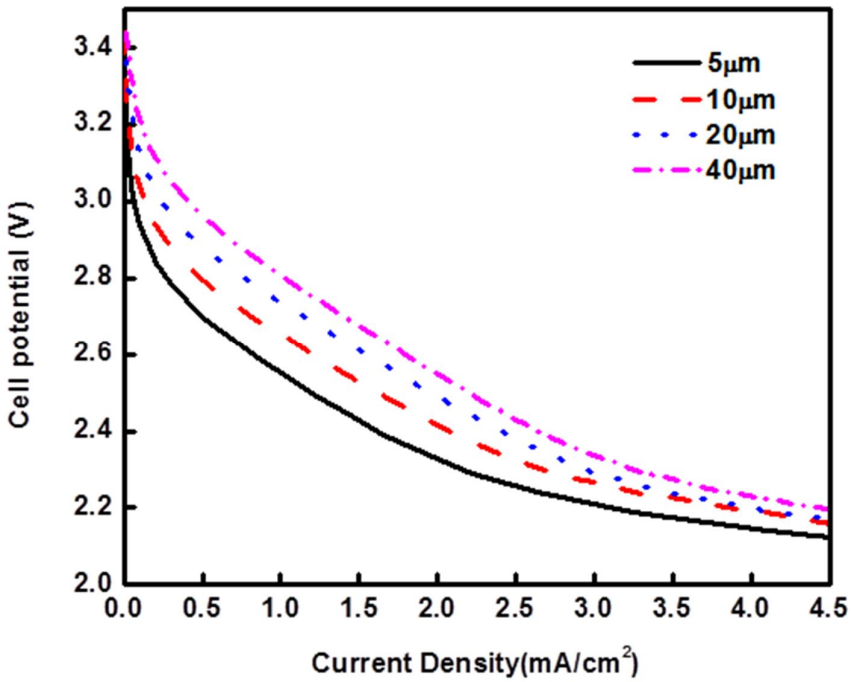

Fig. 3.10 The effect of CNTAs length (L_C) on the performance of the cell under base case.

However, from Fig. 3.10, at relatively larger current densities, the difference in cell performance tends to be smaller. This is because when larger current densities are applied, low oxygen concentrations were observed at the bottom area of the CNTAs. Most of the oxygen is consumed at the top of the reaction sites, and the lower reaction sites are not fully utilized, resulting in reduced cell performance difference. This conclusion can be proved by the OPWC, whose oxygen diffusion limitation is more severe. Fig. 3.11 shows that when the CNTAs length increases from 5μm to 40μm, the current density increases correspondingly in the smaller overpotential region. This is

because at the bottom of the CNTAs, there is still some oxygen to consume which prompts the utilization of the reaction sites. But at larger operation overpotentials, the cell will maintain the same performance, resulting from the insufficient supply of oxygen at the bottom of the CNTAs. So when oxygen is sufficient, increasing CNTAs length can increase the cell performance. When oxygen transport limitation is dominant，the increase of length will be useless.

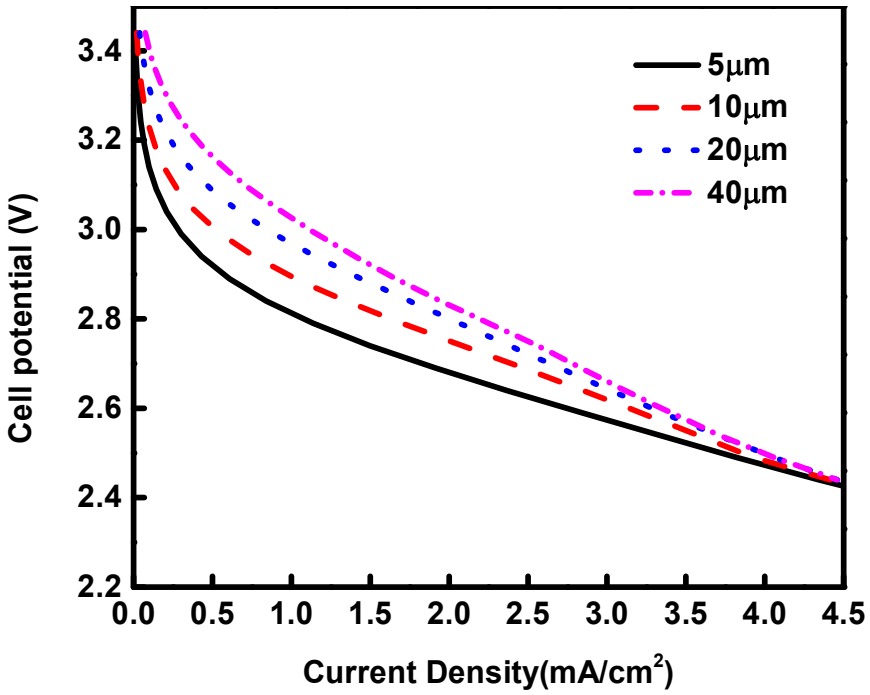

Fig. 3.11 The effect of CNTAs length (L_C) on the performance of the cell under OPWC.

3.2.4. Effect of CNTAs density (d_{CNTAs})

The density of the CNTAs is chosen as 1×10^6 cm^{-2}, 1×10^7 cm^{-2} and 1×10^8 cm^{-2}. Meanwhile, all other structural parameters are as same as the base case. The parameters are listed below.

Table 3.5 Four cases with different CNTAs densities

Case Number	d_{CNTAs} (m^{-2})
1	10^{10}
2	10^{11}
3	10^{12}

The effect of CNTAs density on the performance of the cell is shown in Fig. 3.12. As the density of the CNTAs increases, the cell performance also improves considerably. This is due to the amount of reaction sites per unit area increases when the density value grows. More reaction sites helps the usage of the oxygen in the reaction domain. As a result, increasing density can render better performance of the cell under this current density range.

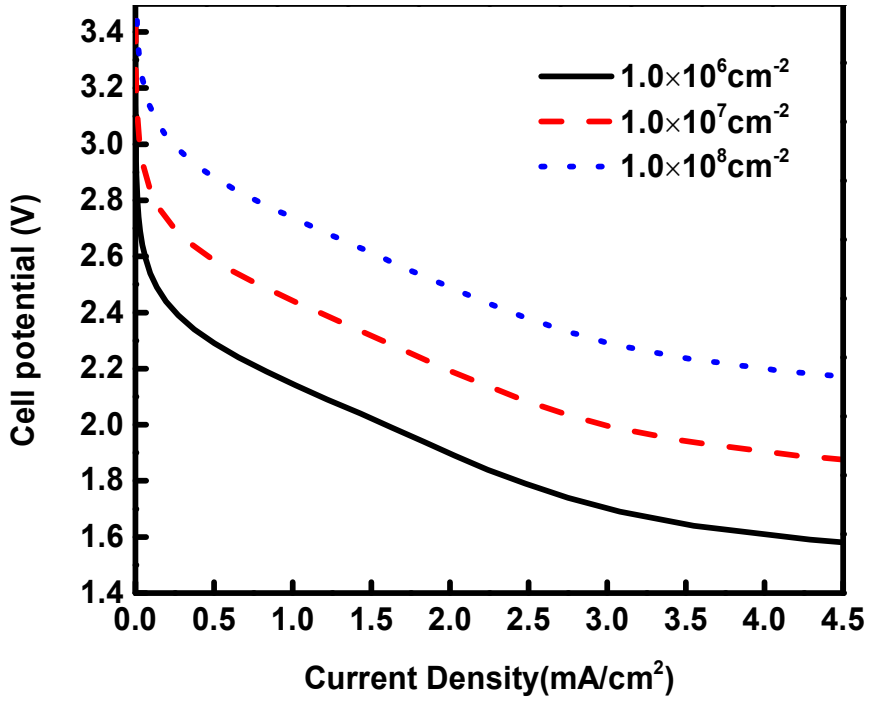

Fig. 3.12 The effect of CNTAs density (d_{CNTAs}) on the performance of the cell under base case.

The effect of CNTAs density on the performance of the cell under OPWC is shown in Fig. 3.13. When the CNTAs' density grows from 1×10^{7} cm^{-2} to 1×10^{8} cm^{-2}, the two lines tend to converse at larger current density region which means that the CNTAs' density starts to decrease its effect. Because at smaller pore width, the oxygen diffusion limitation is more significant at larger current density region. When simply increasing the current density, one will have to face the oxygen diffusion limitation issue especially at the inner area of the reaction domain where there is a lack of oxygen. In other words, we can expect a maximum density of the CNTAs. However, after the maximum point, the cell performance would not be improved anymore.

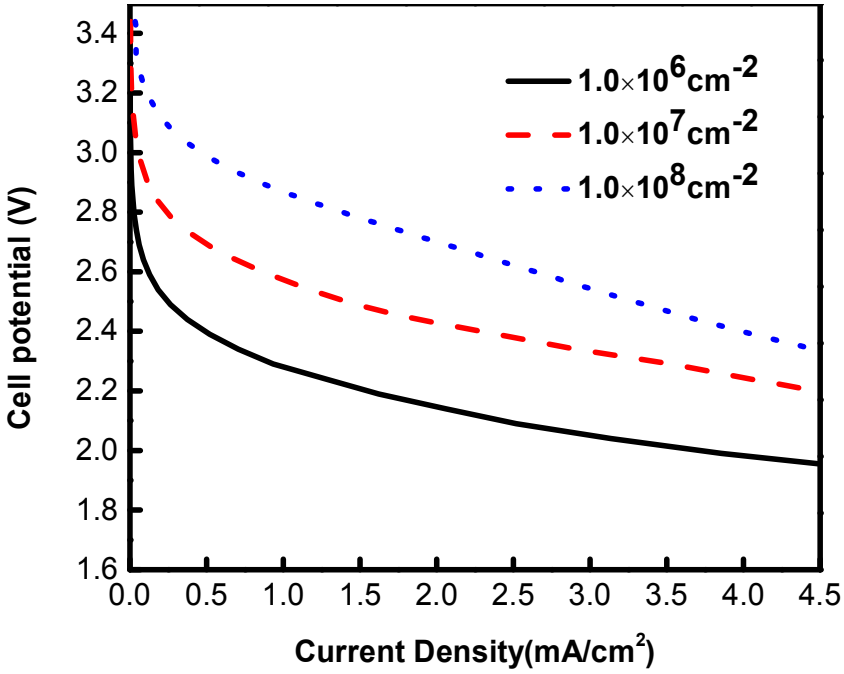

Fig. 3.13 The effect of CNTAs density (d_{CNTAs}) on the performance of the cell under OPWC.

Chapter 4. CONCLUSION AND FUTURE WORK

4.1. Conclusion and summary

Li-air batteries have the potential to be the best candidates for energy storage devices. There is a lot of research that has been done recently. Our has demonstrated a new hierarchical cathode of the aqueous Li-air battery (Li, Huang et al. 2013). A mathematical model of this kind of cathode was developed using the mass transport equations during the discharge of the cells. The established model was compared with our experimental data to justify its validation. Four structure parameters were studied to evaluate their effects on the performance of the cell.

I) There is an optimum backing layer pore width under fixed operating potential, because decreasing pore width will increase the total number of CNTAs within unit area and, on the other hand, impede the oxygen transport.

II) When oxygen is sufficient in the electrolyte, increasing the CNTAs length and density will give better performance. However, if oxygen concentration is limited, increasing the CNTAs length and density will be useless.

III) Although the backing layer thickness has minor influence on the performance of the cell, it is recommended that the thickness can be reduced at higher overpotential.

4.2. Future Work

It must be stressed that the work done in this thesis does not cover all the aspects of Li-air battery optimization. More rigorous studies needed to be done in the future.

I) The effects and optimum of the four structure parameters should be further examined by experiments to see if predictions are right.

II) Since we only modeled the cathode part, the whole battery system should be considered in the future.

III) Other parameters such as the temperature, solubility, external air pressure and so on can be investigated.

IV) It will be more interesting if a time dependent model is built upon the existing model. During the charge and discharge cycles, side reactions and the corrosion of materials do exist and influence the batteries' performance, life time and safety.

Reference

(EIA), U. S. E. I. A. (2012). "Annual Energy Outlook 2012." (DOE/EIA-0383(2012).

A.J. Bard, L. R. F. (2001). "Electrochemical Methods: Fundamentals and Applications, 2nd edition." John Wiley, New York.

B. McCloskey, D. B., R. Shelby, G. Girishkumar, and A. Luntz (2011). The Journal of Physical Chemistry Letters **2**(1161).

Balaish, M., A. Kraytsberg and Y. Ein-Eli (2014). "A critical review on lithium-air battery electrolytes." Phys Chem Chem Phys **16**(7): 2801-2822.

Christensen, J., P. Albertus, R. S. Sanchez-Carrera, T. Lohmann, B. Kozinsky, R. Liedtke, J. Ahmed and A. Kojic (2012). "A Critical Review of Li/Air Batteries." Journal of The Electrochemical Society **159**(2): R1.

D.M. Bernardi, M. W. V. (1991). AIChE J. 37 (1991) **37**(1151).

D.M. Bernardi, M. W. V. (1992). J. Electrochem. Soc. **139**(2477).

Eberle, D. U. and D. R. von Helmolt (2010). "Sustainable transportation based on electric vehicle concepts: a brief overview." Energy & Environmental Science **3**(6): 689.

Elliot, A. J., M. P. Chenier and D. C. Ouellette (1990). "Solubilities of hydrogen and oxygen in concentrated lithium salt solutions." Fusion Engineering and Design **13**(1): 29-31.

G. M. Veith, J. N., J. Y. Howe, and N. J. Dudney (2011). Journal of Physical Chemistry C **155**(14325).

Girishkumar, G., B. McCloskey, A. C. Luntz, S. Swanson and W. Wilcke (2010). "Lithium−Air Battery: Promise and Challenges." The Journal of Physical Chemistry Letters **1**(14): 2193-2203.

Hanpin Luo, J. C., Zhongyao Wu, Chuhang Yang, Yangyang Zheng and Tianfeng Zhao (2012). "Simulation Research on Brushless DC Motor of Electric Car." 2nd International Conference on Electronic & Mechanical Engineering and Information Technology.

Jiang, K. M. A. a. Z. (1996). "A Polymer Electrolyte-Based Rechargeable Lithium/Oxygen Battery." J. Electrochem. Soc **143**(1): 1-5.

John Newman, K. E. T.-A. (2004). "Electrochemical Systems." John Wiley, New York.

Kraytsberg, A. and Y. Ein-Eli (2011). "Review on Li–air batteries—Opportunities, limitations and perspective." Journal of Power Sources **196**(3): 886-893.

Li, X. and A. Faghri (2012). "Optimization of the Cathode Structure of Lithium-Air Batteries Based on a Two-Dimensional, Transient, Non-Isothermal Model." Journal of the Electrochemical Society **159**(10): A1747-A1754.

Li, Y., K. Huang and Y. Xing (2012). "A hybrid Li-air battery with buckypaper air cathode and sulfuric acid electrolyte." Electrochimica Acta **81**: 20-24.

Li, Y., Z. Huang, K. Huang, D. Carnahan and Y. Xing (2013). "Hybrid Li-air battery cathodes with sparse carbon nanotube arrays directly grown on carbon fiber papers." Energy & Environmental Science **6**(11): 3339.

M. K. Tham, R. D. W., and K. E. Gubbins (1970). "Diffusion of Oxygen and Hydrogen in Aqueous Potassium Hydroxide Solutions." J. Phys. Chem. **74**(8): 1747–1751.
Mason, T. R. M. a. E. A. "Gaseous Diffusion Coefficient."

Neetu Meena, V. B., Alka Dubey,Urmila Brighu and Jyotirmay Mathur (2014). "Need and Comparison of Energy Storage Technologies - A Review." International Journal of Applied Engineering Research. **9**(2): 177-184.

R.B. Bird, W. E. S., E.N. Ligthfoot (2007). "Transport Phenomena." John Wiley, New York: 515.

Rao, S. M. and Y. Xing (2008). "Simulation of nanostructured electrodes for polymer electrolyte membrane fuel cells." Journal of Power Sources **185**(2): 1094-1100.

Richter, B. G., D.; Crabtree, G.; Glicksman, L.; Goldstein,, D. K. D.; Greene, D.; Levine, M.; Lubell, M.; Savitz, M.; and D. Sperling (2008). "Energy Future: Think Efficiency." American Physical Society.

S. A. Freunberger, Y. C., Z. Peng, J. M. Griffin, L. J. Hardwick, F. Barde, P. Novak, and P. G. Bruce (2011). Journal of the American Chemical Society **133**(8040).

Tartaglia, A., G. Fracastoro, C. Mele and M. L. Ruggiero (2014). "The role of renewables in the energy crisis." E3S Web of Conferences **2**: 02003.

W. Xu, V. V. V., D. Wang, S. A. Towne, J. Xiao, Z. Nie, D. Hu, and J. G. Zhang (2011). Journal of Power Sources **196**(3894).